nature synthesis

Article

https://doi.org/10.1038/s44160-026-01024-5

Dilute alloy electrocatalysts enable asymmetric C–C coupling for ethylene production from a CO_2 post-capture liquid

Received: 24 November 2024

Accepted: 13 February 2026

Published online: 10 March 2026

Check for updates

Yuanjun Chen[1,2,11], Peiying Wang[1,2,3,11], Yu Mao[4,11], Guangcan Su[1,2,5,11], Hengzhou Liu[1,2], Bosi Peng[1,2], Zeyan Liu[1,2], Huajie Ze[1,2], Yong Wang[1,2], Xiaobing Hu[6,7], Jiantao Li[1], Lizhou Fan[8], Ammar Alahmed[9], Aqil Jamal[9], Issam Gereige[9], Sungsik Lee[10], Jennifer B. Dunn[5], Ziyun Wang[4] ✉, Ke Xie[1,2] ✉ & Edward H. Sargent[1,2] ✉

Direct air capture of CO_2 often uses alkali hydroxides to form carbonate; however, releasing CO_2 and regenerating alkali hydroxides requires an energy-intensive thermal cycle at ~900 °C. Reactive capture systems instead seek to integrate CO_2 release with its chemical reduction in the pathway to fuels and chemicals. Here we focus on a purely electrosynthetic route, beginning by examining why previous attempts at electrified ethylene synthesis from carbonate post-capture liquids have suffered from low overall energy efficiencies. We find that a hydrophilic environment and limited rate of CO_2 generation in situ lead to low CO_2 availability and consequently low *CO coverage on the catalyst surface, and that this hinders C–C coupling. We identify dilute alloy catalysts that implement asymmetric CO–CHO coupling, a lower-barrier route to C–C coupling compared with the conventional symmetric pathway. We report a 51% ± 2% ethylene Faradaic efficiency, a 66 wt% ± 2% concentrated ethylene stream and a 20% end-to-end energy efficiency at 200 mA cm^{-2}. The energy efficiency is a twofold improvement over the most efficient prior report of ethylene production via electrified reactive capture.

CO_2 capture from the atmosphere, paired with electrochemical conversion powered using renewable electricity, offers a route to reduce the carbon intensity of fuels and chemicals[1–3]. Ethylene is an intermediate of interest, with a global market of 150 million metric tons annually[4,5].

One established approach to synthesize ethylene from atmospheric CO_2 follows a sequential process: CO_2 is first extracted and concentrated via direct air capture (DAC), then converted electrochemically in a gas-fed electrolysis (Fig. 1a, Route 1). In widely deployed DAC systems, CO_2 is captured by an alkaline medium such as potassium hydroxide (KOH), yielding a carbonate solution. This carbonate is subsequently processed through a calcium-mediated regeneration loop, which recovers the alkaline sorbent while generating a purified, concentrated CO_2 stream[3,6,7]. A key energy-intensive step in this loop is calcination, occurring at temperatures near 900 °C and demanding 8–10 GJ per tonne of captured CO_2. When scaled to ethylene production, this contributes an estimated 25–31 GJ per tonne of ethylene solely from the carbon feedstock supply[6].

In reactive capture, an approach that seeks to integrate CO_2 capture and upgrade (Fig. 1a, Route 2), the electrochemical system implements CO_2 release as well as electroreduction and enables the production of a substantially CO_2-free outlet stream. Because unreduced CO_2 remains in the captured state, this additional benefit simplifies product separation[8–12]. This route holds great promise to decrease the energy intensity of renewable ethylene production compared

A full list of affiliations appears at the end of the paper. . ✉e-mail: ziyun.wang@auckland.ac.nz; ke-xie@northwestern.edu; ted.sargent@northwestern.edu

https://doi.org/10.1038/s44160-026-01024-5

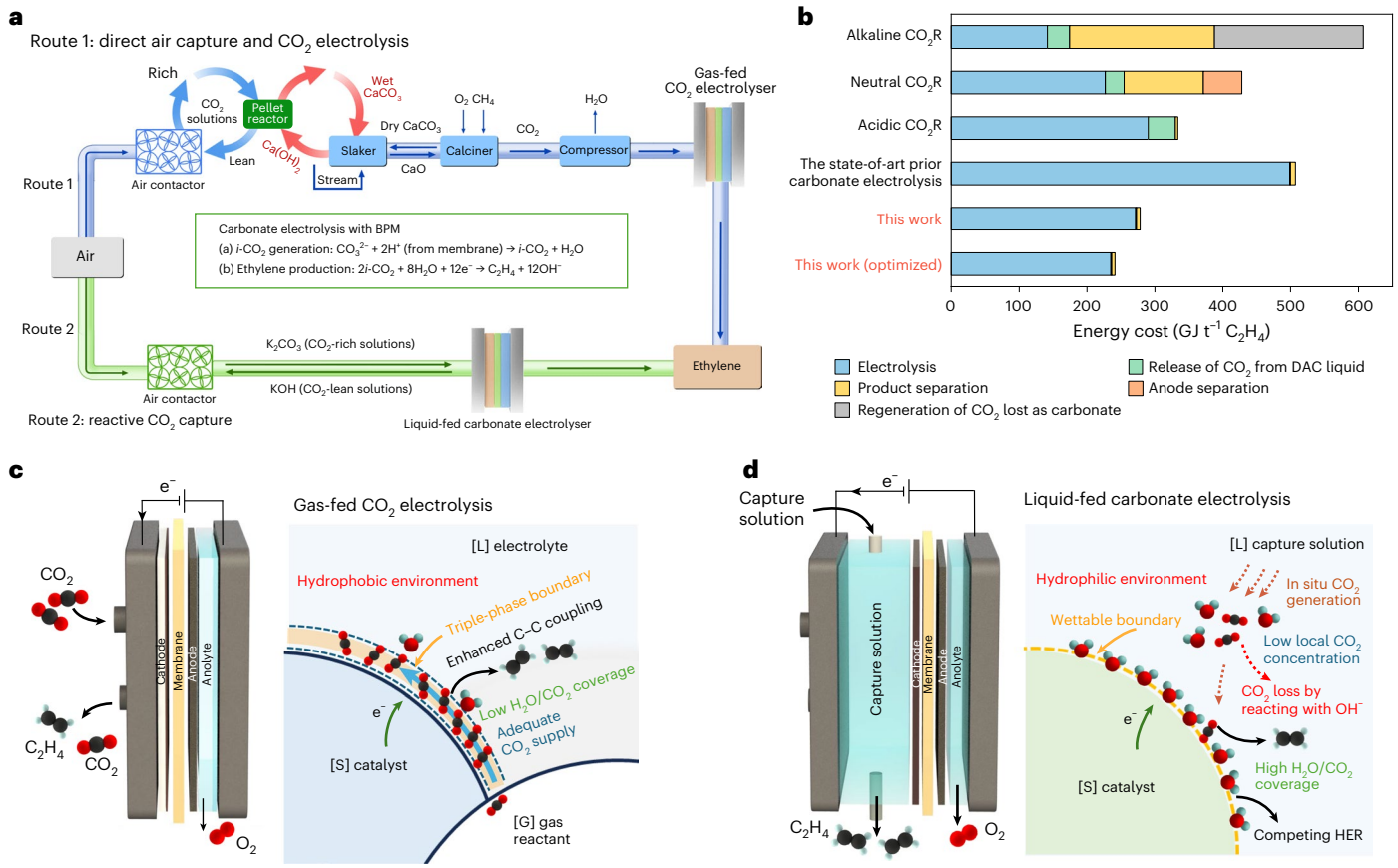

Fig. 1 | Electrosynthesis of ethylene by using captured CO_2 from air. **a**, Schematic illustration of the sequential route of DAC coupled with CO_2 electrolysis (Route 1) and the integrated route of reactive CO_2 capture (Route 2). **b**, Energy expenditure for C_2H_4 production in this work, the prior best-efficient carbonate electrolysis system[11] and the-state-of-the-art literature low-temperature gas-fed CO_2R systems, including alkaline CO_2R[13], neutral CO_2R[14] and acidic CO_2R[15]. **c**, The MEA electrolyser configuration and the local reaction environments of gas-fed CO_2 electrolysis systems. **d**, The MEA electrolyser configuration and the local reaction environments of liquid-fed reactive capture carbonate electrolysis systems. [L], liquid phase; [G], gas phase; [S], solid phase.

with the best prior low-temperature gas-phase CO_2 reduction (CO_2R) in alkaline[13], neutral[14] and acidic[15] systems (Fig. 1b, Supplementary Notes 1 and 2, Supplementary Fig. 1 and Supplementary Tables 1–3). In such liquid-fed carbonate electrolysers, CO_2 is generated in situ via carbonate acidification near the cathode surface and then is electrochemically reduced[9]. Water dissociation in a bipolar membrane (BPM) junction generates protons that migrate through the cation-exchange layer (CEL) under reverse bias[16–19] (Fig. 1a, Route 2).

Reactive capture raises new challenges compared with gas-phase CO_2 electrolysis. In the latter, a catalyst layer on a hydrophobic gas-diffusion layer provides ready access to gas-phase CO_2 reactant[20] (Fig. 1c). The hydrophobic reaction environment enables a high CO_2 supply, and the limited presence of H_2O works against the competing hydrogen evolution reaction (HER). By contrast, a liquid-fed reactive capture carbonate electrolysis system requires a hydrophilic environment for mass transport of the liquid reactant to the catalyst surface (Fig. 1d). Liquid-fed reactive capture carbonate electrolysis systems rely on the in situ generation of CO_2 (i-CO_2), achieved by protonating carbonate (Supplementary Note 3 and Supplementary Figs. 2–6). This presents a challenge: i-CO_2 generation requires acidic conditions on the cathode side of the BPM, while the desired i-CO_2 reduction reaction requires alkaline conditions at the catalyst surface to suppress competing HER (Supplementary Notes 4 and 5). This pH gradient leads to parasitic reactions such as recarbonation and competitive proton consumption that deplete the i-CO_2 supply, leading to a CO_2-starved environment at the catalyst surface (Supplementary Note 6 and Supplementary Tables 4–6). The most efficient prior carbonate-to-ethylene reactive capture carbonate electrolysis exhibited an ethylene Faradaic efficiency (FE) of 34% with an ethylene energy efficiency of 9.5% (ref. 11).

Here, we identified that limited CO_2 availability in liquid-fed reactive capture carbonate electrolysis leads to insufficient *CO coverage on the catalyst surface, which hinders the selective C–C coupling necessary for C_2H_4 production, resulting in low ethylene selectivity and energy efficiency. We therefore designed and synthesized a BiCu dilute alloy catalyst that promotes asymmetric CO–CHO coupling, a lower-energy pathway compared with conventional symmetric C–C coupling. Combined experimental and computational analysis suggest that BiCu enhances *CO coverage, suppresses the competing HER and steers key intermediates towards ethylene under CO_2-starved reaction environments. By further integrating BiCu with a Ni single-atom (Ni-SA) catalyst in a tandem electrode configuration to locally enhance *CO concentration, we achieved an ethylene FE of 51% ± 2% and an overall energy efficiency of 20% at 200 mA cm^{-2}. The increased C_2H_4 FE and nearly 100% CO_2 utilization resulted in a 66 wt% ± 2% C_2H_4 concentration in the outlet stream. Techno-economic assessment indicates an energy cost of ethylene production of 241 GJ t^{-1}, a reduction of over 50% compared with the best prior benchmark of 507 GJ t^{-1}.

Results

We began by studying how low CO_2 availability affects electrolysis using known catalysts, beginning with well-established copper nanoparticle (Cu NP) catalysts (Supplementary Fig. 7). We used a gas-fed system with a low CO_2 partial pressure to mimic the conditions in reactive capture.

From operando Raman spectroscopy, we see three major bands associated with surface-adsorbed *CO at 300–500 and 1,900–2,150 cm^{-1} at an elevated applied potential[21,22] (Supplementary Figs. 8–13). This finding indicates that the *CO coverage on the catalyst surface diminishes with the decrease of local CO_2 concentration. At the same time, the low-frequency band CO, linked with C–C coupling, is diminished[23] (Supplementary Fig. 14). Cu NPs exhibit an increased H_2 FE and a decline in CO FE and ethylene FE as the CO_2 concentration is decreased (Supplementary Figs. 15 and 16). Thus, under CO_2-starved local reaction conditions that reduce CO* coverage, undesired HER is favoured, and this outcompetes the desired C–C coupling.

These considerations motivated us to pursue catalyst designs that improve *CO coverage, suppress HER activity and promote C–C coupling at a low CO_2 partial pressure. We used a microkinetic model to study the dependence of *CO coverage on the CO_2 adsorption energy (G_{ads}(*CO_2)) and CO_2 partial pressure ($P(CO_2)$) (Fig. 2a). We obtain a volcano-shaped relationship between CO_2 adsorption energy (G_{ads}(*CO_2)) and *CO coverage, with an optimal range of 0.2–0.4 eV. This reflects a balance between efficient CO_2 activation and the need for surface sites available to transform the relevant intermediates (*CO_2 ↔ *COOH ↔ *CO) (see details in Supplementary Note 7, Supplementary Fig. 17 and Supplementary Table 7).

On pure Cu, G_{ads}(*CO_2) is 0.6–0.8 eV, which is sufficient for gas-phase CO_2 electrolysis given its high CO_2 partial pressure (Fig. 2a, top right corner). In liquid-fed reactive capture carbonate electrolysis, however, the CO_2 partial pressure is approximately two orders of magnitude lower, and the *CO coverage drops to a level that limits C–C coupling. Hence, strengthening G_{ads}(*CO_2) in the liquid-fed system becomes a priority to achieve a level of *CO coverage comparable to that of pure Cu in the gas-phase CO_2R system (Fig. 2a). Because HER is most active when G_{ads}(*H) approaches 0 eV (ref. 24), we target catalysts having G_{ads}(*H) far from 0 eV, ideally >0.2 eV away.

With these two criteria, we contemplate Cu catalysts incorporating a library of candidate guest metals to form single-atom metal-doped Cu-based binary dilute alloys, calculating their G_{ads}(*CO_2) and G_{ads}(*H) (Fig. 2b). Cu is situated in the top right corner, indicating weak G_{ads}(*CO_2) and nearly 0 G_{ads}(*H). Most single-atom metal-doped Cu dilute alloys enhance CO_2* and H* adsorption, and it is BiCu that appeared the most promising, with G_{ads}(*CO_2) in the range of 0.2–0.4 eV and strong G_{ads}(*H) lower than −0.2 eV.

The computational analysis also identified controls of interest: SnCu and InCu are expected to suppress HER but are predicted to be less effective at CO_2 adsorption, whereas FeCu appears promising for enhanced CO_2 adsorption but may be limited in HER suppression.

We synthesized BiCu dilute alloys, targeting a porous structure through solvothermal-electrochemical reduction (Fig. 2c). We also synthesized SnCu, InCu and FeCu, analogously, for comparison.

We studied BiCu using in situ X-ray absorption spectroscopy (XAS) to investigate the structural evolution from Bi–CuO precatalyst to BiCu catalyst in situ during electrochemical reduction. The binding energies of normalized adsorption peaks in the Cu K-edge X-ray adsorption near-edge spectra shifted from 8,986 eV at open circuit potential to 8,981 eV under in situ electrochemical reduction of 50 mA cm^{-2} at −0.7 V versus reverse hydrogen electrode (RHE) (Supplementary Fig. 18), consistent with Cu entering into the metallic state. In the Cu K-edge extended X-ray absorption fine structure (EXAFS) spectra, the peak at 1.5 Å associated with Cu–O coordination disappeared after reduction, and the peak at 2.2 Å associated with Cu–Cu coordination emerged (Supplementary Fig. 19). Scanning electron microscopy (SEM), transmission electron microscopy (TEM) and high-angle annular dark-field scanning transmission electron microscopy (HAADF-STEM) images show a porous morphology (Fig. 2d and Supplementary Figs. 20 and 21). A lattice spacing of 0.21 nm was observed in high-resolution TEM (HRTEM) (Fig. 2e), and this was associated with the Cu (111) plane. Energy-dispersive X-ray spectroscopy (EDS) shows—within its spatial resolution of 50 nm—a uniform dispersion of Bi and Cu (Fig. 2f). Atomic-resolution HAADF-STEM images, together with three-dimensional atom-overlapping Gaussian-function fitting maps and corresponding intensity profile analysis, suggest the presence of isolated Bi atoms in a Cu matrix, consistent with a dilute dispersed state of Bi species within the Cu matrix, that is, BiCu dilute alloys (Fig. 2g,h and Supplementary Figs. 22 and 23).

We studied BiCu compared with Cu, initially in a gas-fed CO_2 electrolysis reactor, taking advantage of the ability to vary the partial pressure—and thus the availability—of CO_2 over a wide range (Fig. 3a and Supplementary Fig. 24). At a high partial pressure, 50%, BiCu is slightly superior in FE to ethylene compared with Cu (55% instead of 45%). The margin widens considerably at a 10% CO_2 partial pressure, with BiCu remaining above 40%, but Cu declining to 10–15%.

We returned to Raman to look at adsorbates in each case. The 1,900–2,150 cm^{-1} band, associated with surface-bonded CO stretching, appears at lower applied potentials (Fig. 3b) in the case of BiCu than in the case of Cu. The Cu–CO stretch bands in the 300–500 cm^{-1} rregion are blueshifted on BiCu compared with Cu, consistent with stronger CO binding to the BiCu surface[25]. The peak at 1,132 cm^{-1} is associated with the C–H vibrational band of *CHO (ref. 26). A corresponding peak at 1,128 cm^{-1} was observed on BiCu. Charge density difference and crystal orbital Hamilton population analysis offer an account of this observed redshift of the *CHO band on BiCu, linking it to electronic structure changes induced by Bi doping, which correlates with intermediate stabilization and enhanced reaction facilitation (Supplementary Fig. 25 and Supplementary Note 8). Peaks at 973 cm^{-1} and 1,278 cm^{-1} associated with *OCCHO were also detected on BiCu[27]. The Raman spectra of BiCu exhibited stronger *CHO and *OCCHO signal intensities than those of pure Cu, suggesting that Bi doping increases accumulation of the *CHO intermediate and contributes to its asymmetric coupling with *CO to form the intermediate *OCCHO, promoting C_2H_4 production.

We performed in situ electrochemical attenuated total reflection surface-enhanced infrared absorption spectroscopy (ATR-SEIRAS) measurements (Supplementary Figs. 26 and 27). We assign the set of bands observed in the region of approximately 2,150–2,000 cm^{-1} to the C–O stretching vibration of the *CO intermediate[28–30]. The intensity of the *CO band observed on BiCu is higher than that on Cu. As the applied voltage is increased, corresponding to an acceleration of the catalytic reaction rate, the *CO signal on Cu weakens progressively and nearly vanishes. By contrast, the *CO signal on BiCu remains pronounced. From these observations, we offer that BiCu facilitates CO_2 conversion to CO, leading to a higher coverage of *CO on the surface. We assign the features near 1,250 cm^{-1} and 1,180 cm^{-1} to *CHO and *OCCHO, respectively[28]. Notably, the intensities of *CHO and *OCCHO bands are stronger on BiCu relative to Cu. We propose that BiCu enhances the accumulation of the *CHO intermediate and facilitates its asymmetric coupling with *CO to form the intermediate *OCCHO for C_2H_4 production.

The findings from Raman spectra and ATR-SEIRAS prompted us to revisit density functional theory (DFT) calculations to study the possibility that *CO and *CHO could couple to *OCCHO, and whether this might be favoured in the case of BiCu. From charge density difference analysis, Bi produces a surface charge reconfiguration, leading to the formation of an area with enhanced electron distribution surrounding the Bi dopant atom (Supplementary Fig. 28). From the density of states (DOS) analysis (Fig. 3c), Bi doping shifts the *d*-band of Cu proximate Bi towards the Fermi level, consistent with charge analysis showing that Bi enhances the reactivity of nearby Cu atoms. We then calculated the free energy profiles of CO_2 to C_2H_4 (Fig. 3d and Supplementary Figs. 29–32) and found that BiCu exhibits a lower overall free energy profile than that of Cu, with the greatest benefits accrued in CO_2-to-*CO activation and *CO–*CHO coupling.

In Fig. 3e, we focused on specific elementary steps of interest: Bi doping strengthens G_{ads}(*H) from 0.03 eV to −0.35 eV and decreases the

https://doi.org/10.1038/s44160-026-01024-5

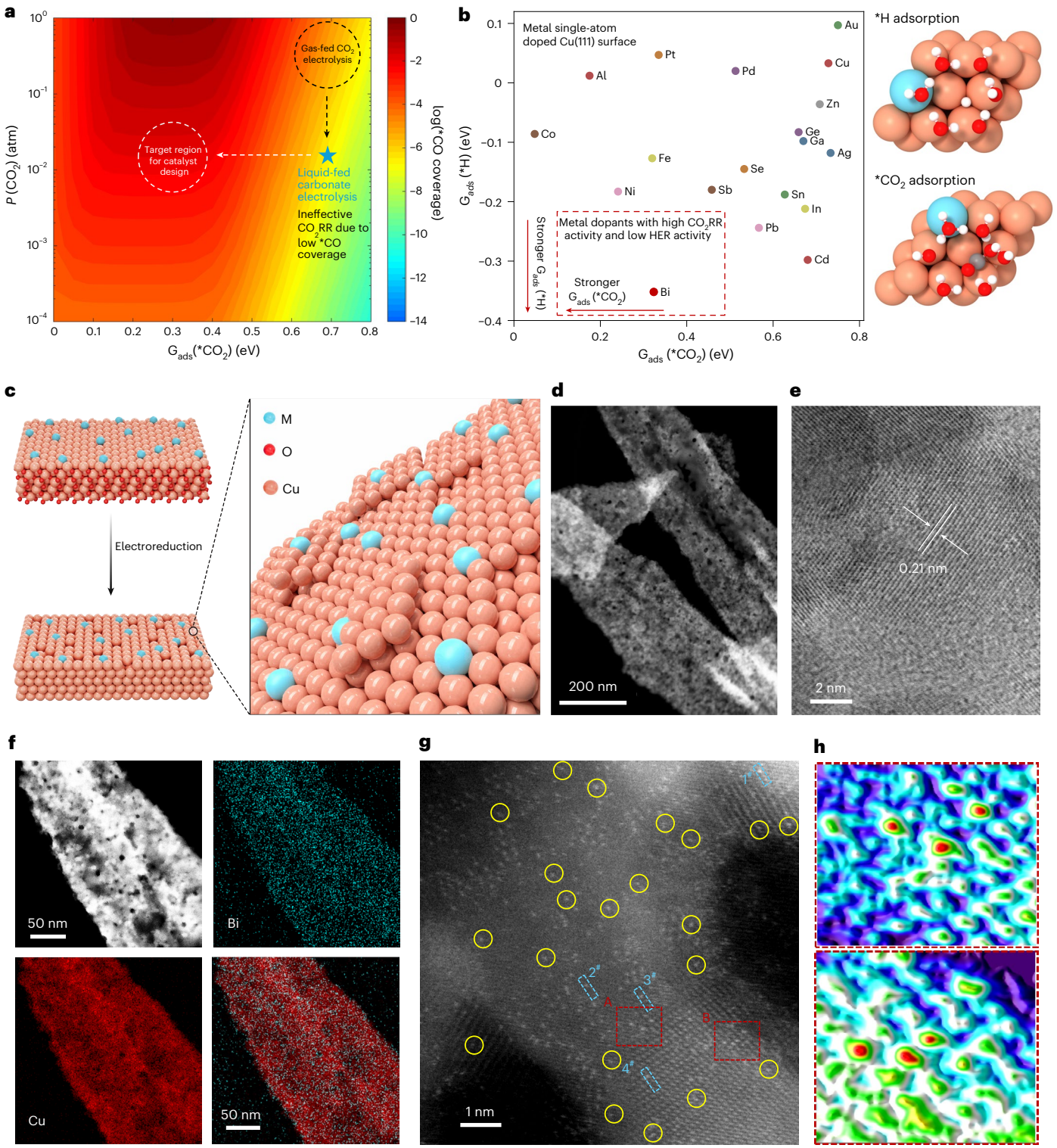

Fig. 2 | Catalyst design for CO_2-starved local environment. a, Two-dimensional map of the *CO coverage with respect to and G_{ads}(*CO_2) and $P(CO_2)$. Deep red represents full coverage. **b**, Computational screening of possible Cu-based dilute alloys with single-atom doping for CO_2-starved local environment. Inserts are the structures of H and CO_2 adsorption considered in DFT calculations. CO_2RR, CO_2 reduction reaction. Red, white, grey, brown and celadon blue represent O, H, C, Cu and doping metal Bi. **c**, Schematic illustration of the preparation of BiCu catalyst. **d**, HAADF-STEM image of BiCu catalyst. **e**, HRTEM image of BiCu catalyst. **f**, EDS element maps of BiCu catalyst. **g**, Atomic-resolution HAADF-STEM images of BiCu catalyst. Isolated bright dots, corresponding to individual Bi atoms, are highlighted by yellow circles. The light-blue rectangles mark the regions from which intensity profiles were extracted; the corresponding profiles are shown in Supplementary Fig. 22. **h**, Three-dimensional atom-overlapping Gaussian function fitting maps. The top and bottom panels correspond to the rectangular dashed red areas labelled A and B in **g**, respectively.

https://doi.org/10.1038/s44160-026-01024-5

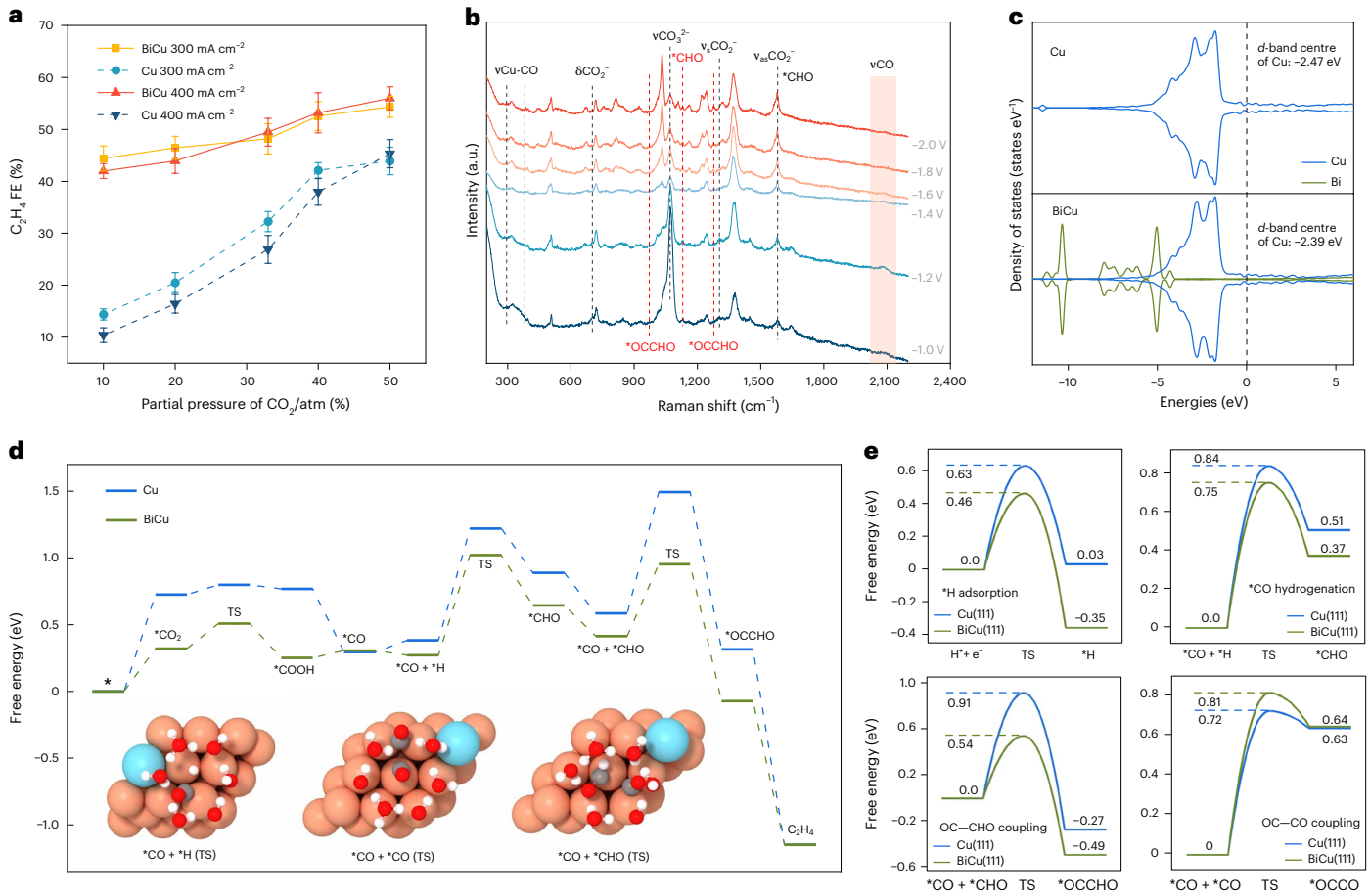

Fig. 3 | Catalytic behaviour of BiCu catalysts studied using dilute gas-fed electrocatalytic performance and operando Raman. a, FEs of C_2H_4 on BiCu versus Cu catalyst at constrained CO_2 availability, a study enabled by varying partial pressure of CO_2. The values are means, and error bars represent the standard deviation from three independent measurements. **b**, Operando Raman spectra of BiCu at constrained CO_2 availability under different potentials versus Ag/AgCl. **c**, The DOS plots of BiCu and Cu surface. **d**, Free energy profile for the CO_2-to-C_2H_4 on BiCu and Cu surface. Inserts are transition state structures for BiCu. **e**, Free energy profiles of *H adsorption, *CO hydrogenation, OC–CHO coupling and OC–CO coupling over BiCu and Cu (111) surface. All energies are calculated at 0 V versus RHE.

*H adsorption barrier from 0.63 eV to 0.46 eV, consistent with suppressing HER and increasing surface *H coverage, as G_{ads}(*H) is substantially lower than 0. As shown in Fig. 2a,b, BiCu retains substantial *CO coverage even under low CO_2 partial pressure due to enhanced G_{ads}(*CO_2). These combined findings suggest that the reaction *CO + H* → *CHO could become appreciable on BiCu. The energy barrier for OC–CO coupling on Cu (0.72 eV) is lower than that for OC–CHO coupling (0.91 eV), suggesting that OC–CO coupling will predominate. On BiCu, the energy barrier for OC–CHO coupling (0.54 eV) is lower than that for OC–CO coupling (0.81 eV). Considering the enhanced *CHO-related intensities observed in both Raman and ATR-SEIRAS spectra, along with lower free energy of *CHO on BiCu, it appears that the OC–CHO coupling step (0.54 eV) is favoured on BiCu (Supplementary Note 9).

Experimentally, in the reactive capture carbonate electrolysis system with K_2CO_3 simulating the post-capture liquid, BiCu showed a peak ethylene FE of 42% ± 3% at 350 mA cm^{-2}, compared with pristine Cu, which exhibited its peak ethylene FE of 18% ± 1% at 300 mA cm^{-2} (Fig. 4a and Supplementary Fig. 33). We also evaluated the performance of SnCu, InCu and FeCu, analogously, for comparison (Supplementary Fig. 34). We found that SnCu, InCu and FeCu showed lower ethylene FE compared with BiCu but higher ethylene FE relative to Cu. The H_2 FE observed on FeCu was higher than those observed on SnCu, InCu and BiCu. When BiCu was used, the ethylene concentration in the outlet stream reached 60 wt%, with the remainder mostly H_2 and CO_2 <0.5% (Supplementary Figs. 35 and 36).

We further tuned the performance of BiCu by integrating it atop a Ni-SA catalyst to construct a Ni-SA/BiCu tandem electrode configuration (Supplementary Figs. 37–39). This led to a peak FE of 47% ± 2% for ethylene (Fig. 4a and Supplementary Figs. 40 and 41). To decrease the full-cell voltage, we used a BPM containing a water dissociation catalyst and a NiFeP foam as the oxygen evolution reaction (OER) catalyst, achieving an ethylene energy efficiency of 17.6% ± 1% at 200 mA cm^{-2} (Fig. 4b). This energy efficiency is 1.8× higher than that of the most efficient prior report of ethylene electrosynthesis in a reactive capture system[11] (Supplementary Fig. 42).

We observed in the present system a carbon utilization of >99.5% across the current density range of 100–400 mA cm^{-2} (Supplementary Fig. 43). Carbon utilization is high because the BPM prevents carbonate crossover to the anode and because most of the in-situ-produced CO_2 is converted into carbon-containing products, resulting in less than 0.5% CO_2 in the gas stream. This carbon utilization compares with 1–10% carbon utilization in alkaline CO_2R electrolysis[13,31], 10–30% in neutral CO_2R electrolysis[14,32] and 70–90% in acidic CO_2R electrolysis[15,33,34]. The 64 wt% ethylene in the tailgas compares with 0.1–5 wt%, 5–50 wt% and 20–50 wt% in alkaline CO_2R, neutral CO_2R and acidic CO_2R systems, respectively (Fig. 4c Supplementary Fig. 44 and Supplementary Table 3). We evaluated initial stability, obtaining 125-h operation (Fig. 4d). Post-stability characterization showed a well-preserved catalyst structure (Supplementary Fig. 45 and Supplementary Note 10).

https://doi.org/10.1038/s44160-026-01024-5

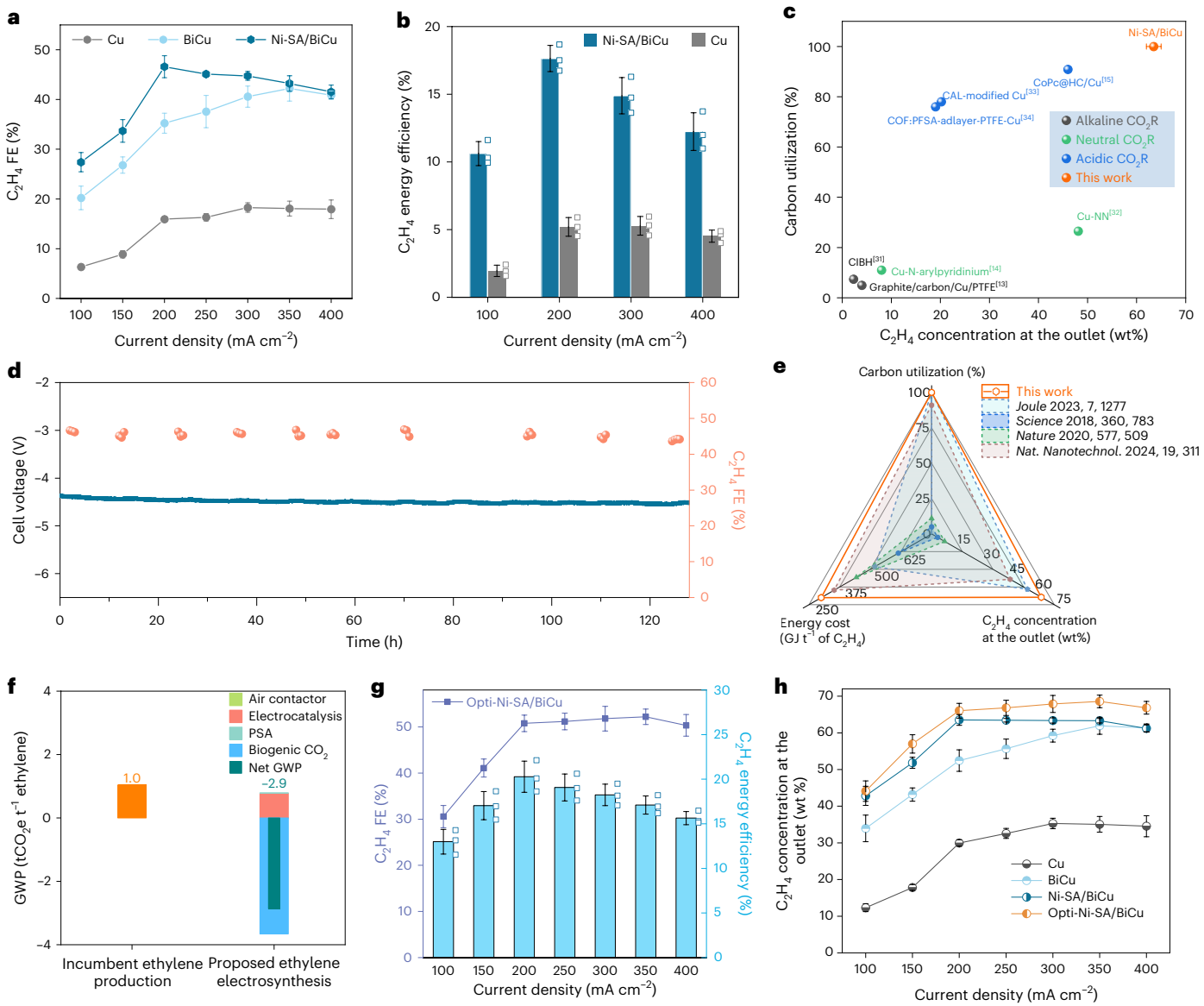

Fig. 4 | Performance of ethylene production in a reactive capture carbonate electrolysis system. a, Comparison of C_2H_4 FE of Cu electrode, BiCu electrode and Ni-SA/BiCu tandem electrode in 1.5 M K_2CO_3 solution in a liquid-fed reactive capture carbonate electrolysis system. **b**, Comparison of C_2H_4 energy efficiency between the Ni-SA/BiCu tandem electrode and Cu electrode. The values are means, and error bars represent the standard deviation from three independent measurements. The corresponding data distribution is presented as hollow points. **c**, C_2H_4 concentration at the outlet and CO_2 utilization in this work and literature benchmark gas-fed CO_2R systems, including alkaline CO_2R (refs. 13,31), neutral CO_2R (refs. 14,32) and acidic CO_2R (refs. 15,33,34). COF, covalent organic framework. **d**, The 125-h stability at a total current density of 200 mA cm^{-2} on the Ni-SA/BiCu tandem electrode using the commercial BPM with NF as the OER catalyst. **e**, Comparison of the carbon utilization, C_2H_4 concentration at the outlet and energy cost for C_2H_4 production of this work with those of state-of-the-art reported works[11,13–15]. **f**, Global warming potential (GWP) values of incumbent ethylene production route and proposed ethylene production route in this work using wind energy. The teal bar is the net GWP value. **g**, C_2H_4 FE and energy efficiency of optimal Ni-SA/BiCu tandem electrode in liquid-fed reactive capture carbonate electrolysis system. The values are means, and error bars represent the standard deviation from three independent measurements. The corresponding data distribution is presented as hollow points. **h**, Comparison of C_2H_4 concentration at the outlet between optimal Ni-SA/BiCu, Ni-SA/BiCu, BiCu and Cu in liquid-fed reactive capture carbonate electrolysis system. The values are means, and error bars represent the standard deviation from three independent measurements.

We evaluated the energy intensity of ethylene production for the reactive capture system compared with those relying on CO_2 capture, release and gas-phase electroreduction (Figs. 1b and 4e, Supplementary Notes 1 and 2 and Supplementary Tables 1 and 2). We estimate ~278 GJ t^{-1} for the reactive capture system, which is 45% lower than that of the highest-efficiency prior report of ethylene electrosynthesis in reactive capture system[11]. This approach also achieves a significant reduction in the energy intensity of ethylene production compared with state-of-the-art gas-phase CO_2R in alkaline, neutral and acidic systems[13–15].

Life cycle assessment shows that greenhouse gas (GHG) emissions can be reduced from today's 1.04 t CO_2 equivalents (CO_2e) t^{-1} ethylene (from steam cracking of natural gas) to a negative emission of −2.86 t CO_2e t^{-1} ethylene in our system, when CO_2 is sourced from DAC and then electrochemically upgraded into ethylene, and subsequently purified by pressure-swing adsorption (PSA), all powered by wind electricity (Fig. 4f, Supplementary Fig. 46 and Supplementary Note 11).

In the studies up to this point, we used liquid K_2CO_3. By contrast, a DAC post-capture liquid contains appreciable OH^-, with a pH of

approximately 13.5 (refs. 7,35) (Supplementary Fig. 47). We therefore evaluated our system using a more realistic post-capture liquid with pH 13.5 over a current density range of 150–250 mA cm^{-2}, maintaining a C_2H_4 FE above 40% (Supplementary Fig. 48). By contrast, Cu shows a peak C_2H_4 FE of 16% at 200 mA cm^{-2}. We also checked whether the carbonate electrolyser could return the cathode electrolyte, which can be used for further CO_2 capture in the gas contactor (for capture) and the carbonate electrolyser (for release and upgrade to C_2H_4) system. When electrolysis was operated for 4 h at 200 mA cm^{-2} using a pH 13.5 post-capture liquid, the system maintained approximately 40% C_2H_4 FE and yielded a pH 13.8 post-electrolysis liquid for the next round of capture (Supplementary Fig. 49).

Discussion

We elaborate on the origins of the performance of the Ni-SA/BiCu tandem catalyst (Supplementary Note 12, Supplementary Figs. 50–58 and Supplementary Tables 8–11). *i*-CO_2 diffuses from the BPM and, once it traverses the interposer, is converted to CO by the Ni-SA catalyst layer; the resulting CO then travels inwards to the underlying BiCu layer for C–C coupling into C_2H_4 (Supplementary Fig. 58). We place the CO-producing Ni-SA layer on top to enhance the local CO concentration on the BiCu catalyst. Given CO's low solubility in aqueous electrolyte, a concentration gradient enables CO to go downwards through the BiCu layer. This tandem configuration tackles challenges specific to liquid-fed reactive capture carbonate electrolysis systems.

The Ni-SA/BiCu tandem shows a higher CO FE and a higher C_2H_4 FE than BiCu alone (Supplementary Tables 8 and 9), that is, the CO generated on the Ni-SA catalyst layer is well utilized. Electrochemical linear sweep voltammetry measurements show a lower overpotential for the tandem electrode, and we observe higher C_2H_4 partial current densities at lower potentials (Supplementary Figs. 56–58 and Supplementary Note 13). We offer that the Ni-SA layer facilitates the CO_2-to-CO step, lowering the energy barrier for the overall process to C_2H_4. Control experiments comparing the catalytic performance of BiCu under 10% CO_2 versus 10% CO in a gas-fed electrolysis system show that BiCu exhibits higher C_2H_4 FE and lower H_2 FE with 10% CO than with 10% CO_2 (Supplementary Fig. 50). Linear sweep voltammetry measurements show a lower overpotential for BiCu with 10% CO compared with CO_2 (Supplementary Fig. 52). Thus, increasing CO availability enhances C_2H_4 production, reduces overpotential and suppresses the HER.

We sought to use this insight to further improve C_2H_4 production. We optimized Ni-SA/BiCu tandem electrodes by varying the mass loading of the Ni-SA catalyst to regulate CO availability in the liquid-fed reactive capture carbonate electrolysis system (Supplementary Figs. 60 and 61). The optimal Ni-SA/BiCu tandem electrode (Opti-Ni-SA/BiCu) achieved a 51% ± 2% C_2H_4 FE and a 20% overall energy efficiency at 200 mA cm^{-2}, delivering a 66 wt% concentrated C_2H_4 stream (Fig. 4g,h and Supplementary Figs. 62–64). This energy efficiency is improved 2× over that of most efficient prior reports, that is, the estimated total energy cost of C_2H_4 production is ~241 GJ t^{-1} instead of 507 GJ t^{-1} in the highest-efficiency prior report of ethylene electrosynthesis in an electrified reactive capture system (Supplementary Fig. 65). Cradle-to-gate life cycle assessment indicates that, with this optimal catalyst, the system could reduce GHG emissions from today's 1.04 tCO_2e t^{-1} ethylene to −3.0 tCO_2e t^{-1} ethylene by using CO_2 from DAC and an electrochemical conversion step, both powered by wind electricity (Supplementary Fig. 66).

Conclusions

In this work, we investigated the origins of limited electrified ethylene synthesis in prior liquid-fed reactive capture carbonate electrolysis systems. We found that the hydrophilic environment and restricted in situ CO_2 generation rate result in low *CO coverage on the catalyst surface, thereby limiting the C–C coupling essential for ethylene formation. To overcome this, we implemented a BiCu dilute alloy catalyst that promotes asymmetric CO–CHO coupling, a lower-barrier pathway than conventional symmetric C–C coupling, enabling efficient ethylene production. Once optimized, the system achieved an ethylene FE of 51% ± 2% from a CO_2 post-capture liquid carbonate to ethylene with nearly 100% CO_2 utilization, producing a concentrated 66 wt% ± 2% ethylene stream and achieving an overall energy efficiency of 20% at 200 mA cm^{-2}, which is 2× that seen in the most efficient prior reports.

Methods

Chemicals

Bismuth(III) chloride ($BiCl_3$), copper(II) nitrate trihydrate ($Cu(NO_3)_2{\cdot}3H_2O$), sodium hydroxide (NaOH), zinc nitrate hexahydrate ($Zn(NO_3)_2{\cdot}6H_2O$), nickel(II) nitrate hexahydrate ($Ni(NO_3)_2{\cdot}6H_2O$), tin(IV) chloride pentahydrate ($SnCl_4{\cdot}5H_2O$), indium (III) chloride tetrahydrate ($InCl_3{\cdot}4H_2O$), iron (III) chloride hexahydrate ($FeCl_3$ $6H_2O$), iron(III) nitrate nonahydrate ($Fe(NO_3)_3{\cdot}9H_2O$), 2-methylimidazole, *N*,*N*-diethylethanamine, NH_4F, urea, sodium hypophosphite ($NaH_2PO_2{\cdot}H_2O$), potassium carbonate (K_2CO_3), potassium hydroxide (KOH), hydrochloric acid, methanol, ethanol, acetonitrile and isopropanol were purchased from Sigma-Aldrich. Phosphonitrilic chloride trimer (98%), and bis(4-hydroxyphenyl) sulfone were purchased from Alfa Aesar. Cu NPs (25 nm) were purchased from US Research Nanomaterials. The commercial BPM (Fumasep FBM) and gas diffusion layers (carbon papers, Freudenberg H23 and Freudenberg H23C3) were purchased from Fuel Cell Store. Nickel foam (thickness 1.6 mm) was obtained from Sigma-Aldrich. Nafion perfluorinated resin dispersion (D520CS, 5 wt%) was purchased from Ion Power. Distilled water (DI-water) with a resistivity of 18.2 MΩ cm was obtained from a Milli-Q reference water purification system.

Material synthesis and electrode preparation

The typical synthesis of BiCu diluted-alloy catalyst is illustrated as an example. In brief, 0.075 mmol of $BiCl_3$ (23.7 mg) was dispersed in a mixture solution containing 4 ml acetonitrile and 1 ml 1.2 M HCl. Then, the mixture solution was added dropwise to 40 ml solution with 5 mmol $Cu(NO_3)_2.3H_2O$ (1,208 mg), which was maintained at or below 4 °C in an ice water bath. Following this, 10.5 ml 2.4 M NaOH aqueous solution was introduced dropwise. The combined mixture was vigorously stirred magnetically for 15 min to achieve a uniform dispersion. It was then transferred to a sealed 100-ml high-pressure steel reactor and heated at 150 °C for 2 h. After cooling, a dark-brown precipitate was collected via centrifugation, washed thoroughly with water and ethanol, and dried under vacuum at 60 °C. The obtained powder was annealed at 400 °C in air for 3 h to obtain Bi–CuO. The catalyst ink was prepared by dispersing 80 mg of the synthesized Bi–CuO powder or Cu NPs (US Research Nanomaterials) in 8 ml of isopropanol and 200 mg of Nafion perfluorinated resin dispersion (5 wt%), followed by sonication to achieve a uniform catalyst dispersion. The catalyst ink was then airbrushed onto the carbon papers (H23 or H23C3), giving a final catalyst loading of 2 mg cm^{-2}. The catalysts on H23 carbon papers were used for liquid-fed reactive capture carbonate electrolysis, while the catalysts on H23C3 carbon papers were used for gas-fed CO_2 electrolysis under the constrained CO_2 availability conditions. The BiCu electrode was finally obtained by an electrochemical reduction of the preformed Bi–CuO running for 30 min at 50 mA cm^{-2} in 1.5 M K_2CO_3 electrolyte in liquid-fed carbonate electrolysis system in a membrane electrode assembly (MEA) electrolyser. The SnCu, InCu and FeCu catalysts were obtained using a similar procedure as BiCu catalyst, except that the $BiCl_3$ was replaced by $SnCl_4{\cdot}5H_2O$, $InCl_3{\cdot}4H_2O$ and $FeCl_3{\cdot}6H_2O$, respectively.

In a typical synthesis of Ni-SA catalyst, ZIF-8 was first prepared by dissolving 6 mmol of $Zn(NO_3)_2{\cdot}6H_2O$ (1785 mg) and 24 mmol of 2-methylimidazole (1,970 mg) separately in 50 ml of methanol. The solutions were then mixed with vigorous stirring for 3 min at room temperature. After mixing, the reaction was allowed to proceed at 35 °C

for 6 h. The precipitates were collected by centrifugation, washed and vacuum-dried at 80 °C to obtain ZIF-8 powder. Next, 400 mg of the as-synthesized ZIF-8 powder was dispersed in 40 ml of methanol via sonication. Subsequently, a methanol solution (100 ml) consisting of bis(4-hydroxyphenyl) sulfone (325 mg) and phosphonitrilic chloride trimer (152 mg) was added to the ZIF-8 dispersion and stirred for 15 min. Then, 1 ml of *N*,*N*-diethylethanamine was slowly introduced dropwise, and the mixture was stirred at room temperature for 15 h. The resulting precipitate, denoted as ZIF-8@PZS, was collected, washed and vacuum-dried at 80 °C for 12 h. The ZIF-8@PZS was the placed in a quartz boat and heated at 650 °C for 2 h in a tube furnace under flowing Ar with a heating rate of 5 °C min^{-1}. Following this, 200 mg of the obtained powder was dispersed in 50 ml of methanol by sonication. Subsequently, 1.98 ml of $Ni(NO_3)_2{\cdot}6H_2O$ (10 mg ml^{-1}) methanol solution was slowly added to this suspension, which was then stirred at room temperature for 24 h at room temperature. The resulting precipitate was collected, washed, dried and then subjected to a final thermal treatment at 1,000 °C for 3 h in a tube furnace under flowing Ar with a heating rate of 5 °C min^{-1}.

For the preparation of the Ni-SA/BiCu tandem electrode, a catalyst ink containing 10 mg Ni-SA catalyst, 2 ml methanol and 30 µl Nafion perfluorinated resin solution was sprayed onto the preformed Bi–CuO electrode with a Ni-SA catalyst loading of 0.5 mg cm^{-2} using airbrushing to obtain the performed Ni-SA/Bi–CuO electrode. The Ni-SA/BiCu tandem electrode was finally obtained by an electrochemical reduction of the preformed Ni-SA/Bi–CuO electrode running for 30 min under reaction conditions at 50 mA cm^{-2} in liquid-fed carbonate electrolysis system in a MEA electrolyser. The optimized tandem electrode was synthesized following an identical procedure but with a Ni-SA catalyst loading of 0.75 mg cm^{-2}.

The optimized anode electrode was prepared using a modified method[36]. First, Ni foam (NF, 2 cm × 4 cm) was sonicated in 6 M HCl, DI-water and ethanol for 30 min, respectively, to remove surface oxides. Then, the cleaned NF was transferred to a 50-ml Teflon-lined stainless-steel autoclave containing a uniformly mixed solution of 2 mmol $Ni(NO_3)_2{\cdot}6H_2O$ (582 mg), 2 mmol $Fe(NO_3)_3{\cdot}9H_2O$ (808 mg), 4 mmol NH_4F (148 mg) and 10 mmol urea (601 mg) in 40 ml of DI-water. The hydroxides were synthesized on NF through hydrothermal growth at 120 °C for 6 h with a heating rate of 3 °C min^{-1}. Subsequently, the NiFe-precursor/NF was washed with DI-water and dried in an oven at 80 °C. To prepare NiFeP, the NiFe-precursor/NF and 1.0 g of $NaH_2PO_2{\cdot}H_2O$ were placed in separate positions within a quartz boat placed inside a tube furnace, with $NaH_2PO_2{\cdot}H_2O$ located upstream in the gas flow. After purging with Ar, the furnace temperature was raised to 300 °C at a ramping rate of 1 °C min^{-1} and maintained for 1 h in an Ar atmosphere. The system was then allowed to cool naturally to room temperature.

Materials characterization

Powder X-ray diffraction spectra were collected in transmission geometry on a STOE-STADI P powder diffractometer operating at 40 kV voltage and 40 mA current with Cu-Kα1 X-ray radiation (λ = 0.154056 nm). Atomic-resolution HAADF images and the high-spatial-resolution energy-dispersive X-ray spectroscopy (EDS) mappings were obtained using JEOL ARM200CF TEM. This microscope was attached with a probe corrector and dual silicon drift detectors. TEM samples were prepared using the drop-cast method. The powders were first scratched off from the cathode surface and then dispersed in 2-propanol. X-ray photoelectron spectroscopy was conducted on a Thermo Scientific NEXSA G2 XPS spectrometer equipped with an Al K alpha radiation source and electron flood-gun at a pressure of 8×10^{-8} mbar with a pass energy of 50 eV. All spectra were calibrated with the C 1*s* peak at 284.8 eV. SEM–EDS was performed using a JEOL JSM-7900FLV scanning electrode microscope. The system, operating at an accelerating voltage of 10 kV in backscattered electron detection mode, is equipped with a light-element X-ray detector and an Oxford Aztec energy-dispersive X-ray analysis system. XAS data were obtained at the 9BM beamline of the Advanced Photon Source (Argonne National Laboratory, Lemont, Illinois). The XAS data were processed using ATHENA and ARTEMIS software within the standard IFEFFIT package. Operando Raman spectra were recorded with a Renishaw inVia Raman spectrometer using an in-house in situ cell and a ×50 water immersion lens. Cu NPs and BiCu catalyst were used as the cathode electrode in 0.5 M K_2CO_3 electrolytes, purged with a mixture of CO_2 and Ar from the backside. Pt wire and Ag/AgCl were used as the anode and reference electrodes, respectively. In situ ATR-SEIRAS measurements were conducted using a BRUKER INVENIO R spectrometer equipped with a liquid-nitrogen-cooled mercury cadmium telluride detector.

Electrochemical measurements

Electrochemical measurements of liquid-fed reactive capture carbonate electrolysis systems were evaluated in the MEA electrolyser (SKU: 68732; Dioxide Materials). Peristaltic pumps (INTLLAB) circulate catholyte and anolyte at 60 ml min^{-1}. The applied current is regulated by a BioLogic potentiostat/galvanostat. A commercial BPM (Fumasep FBM, Fuel Cell Store) or custom-designed BPM separates the catholyte and anolyte. The custom BPM was fabricated by assembling a Nafion 212 CEL, a water-dissociation catalyst layer and a PiperION-A40-HCO3 anion-exchange layer. The CEL was stored in DI-water; the anion-exchange layer was preconditioned in 0.50 M KOH for over 1 h, rinsed and stored in fresh 0.50 M KOH before use. The water-dissociation catalyst ink, prepared by dispersing commercial P25-TiO_2 (Thermo Fisher) in a water/isopropanol mixture (1:1 w/w) to a concentration of 0.2 wt%, was spin-coated onto the CEL at 3,000 rpm for 30 s to form a uniform thin film. The cathode electrode utilizes the as-prepared BiCu catalyst or Ni-SA/BiCu tandem catalyst, with a filter membrane (polytetrafluoroethylene (PTFE), 10 µm) as the interposer layer between the cathode electrode and cation exchange layer. The NF or optimized NiFeP catalyst was used as the anode electrode. The catholyte was 1.5 M K_2CO_3, and the anolyte was 1 M KOH. A flow N_2 carrier gas flow of 50 sccm was maintained through the cathode outlet in all experiments to transport the generated gaseous products (C_2H_4, H_2, CO and so on) for quantitative analysis.

A gas-fed CO_2 electrolysis system was utilized to simulate CO_2-starved environments analogous to a liquid-fed reactive capture carbonate electrolysis system. The gas-fed CO_2 electrolysis system comprised a flow-cell electrolyser with an anion-exchange membrane separating the compartments. The cathode chamber was fed with a 1.5 M K_2CO_3 catholyte, while the reactant gas—a mixture of CO_2 and N_2 with partial pressures ranging from 0.1 to 0.5 atm—was purged over the gas diffusion electrode at a fixed total flow rate of 20 sccm. The anode consisted of a NF OER catalyst immersed in a 1 M KOH anolyte.

The gaseous products, including H_2, CO, CH_4 and C_2H_4 were quantified using a gas chromatograph (Shimadzu2014, PerkinElmer Clarus 580) equipped with a thermal conductivity detector and a flame ionization detector coupled with with a methanizer. Argon served as the carrier gas at a flow rate of 100 ml min^{-1} to transport the gaseous products out of the system for quantification analysis. Quantification was performed on the basis of calibration curves established using standard calibration gases with concentrations ranging from 10 to 10,000 ppm. Liquid products were analysed by ^{1}H nuclear magnetic resonance spectroscopy. The measurements were performed on a 600-MHz Agilent DD2 NMR spectrometer equipped with water suppression mode. Dimethyl sulfoxide served as the reference standard, while deuterium oxide (D_2O) was used as the lock solvent for the analysis.

The FE for each product is calculated according to

$$FE_i = \frac{n_i z_i F}{Q} \times 100\%,$$

where n_i represents the molar quantity of product i; z_i denotes the number of electrons transferred per molecule of the product; F is the Faraday constant (96,485 C mol^{-1}); and Q stands for the total charge passed through the electrolyser.

The carbon utilization is calculated using

$$\text{Carbon utilization} = \left(1 - \frac{n_{\text{CO2 (g)}}}{n^0_{\text{CO2}}}\right) \times 100\%,$$

where n^0_{CO2} represents the theoretically derived moles of CO_2 from the BPM-based electrolyser; and $n_{\text{CO2 (g)}}$ is the total moles of gaseous CO_2 detected at the cathode and anode outlets.

The full-cell energy efficiency (EE) for ethylene production is calculated as

$$\text{EE}_{\text{full cell, ethylene}} = \frac{(1.23 + (-E^0_{\text{ethylene}})) \times \text{FE}_{\text{ethylene}}}{-E_{\text{full cell}}},$$

where E^0_{ethylene} ($E^0_{\text{ethylene}} = 0.08$ V versus RHE) is the thermodynamic potential of CO_2-to-ethylene, $\text{FE}_{\text{ethylene}}$ denotes the measured FE of ethylene, and $E_{\text{full cell}}$ represents the full-cell voltage without ohmic-loss correction, as recorded in the MEA electrolyser.

DFT calculations

All calculations in this Article were spin-polarized and carried out using the Perdew–Burke–Ernzerhof[37] functional in the Vienna ab initio simulation package (VASP)[38,39]. The D3 correction method[40] was used to include van der Waals interactions. The project-augmented wave method was used to represent the core–valence interaction[41,42]. For the calculations of total energy, a cut-off energy of 450 eV was set for the plane-wave basis to expand the valence electronic states, and structural optimizations were performed with a convergence criterion of forces on each relaxed atom below 0.05 eV Å^{-1}. For the modelling of copper, the crystal structure was optimized, yielding an equilibrium lattice constant of 3.63 Å for Cu. A periodic four-layer (3 × 3) Cu(111) model was used, with the bottom layer fixed while the top two layers were fully relaxed during structural optimizations. Metal single-atom doping was realized by replacing one surface Cu atom with another metal atom. At all intermediate and transition states, one charged layer of water molecules was added to the surface to take the combined field and solvation effects into account[43]. The Brillouin zone was sampled 3 × 3 × 1, and a vacuum layer of 15 Å was applied to avoid lateral interactions. Structures are visualized using OVITO[44]. The transition states (TS) were determined using a constrained optimization scheme[45,46] and were verified until (1) all forces on atoms vanished, and (2) the total energy reached a maximum along the reaction coordinate but a minimum with respect to the remaining degrees of freedom.

The adsorption energy (ΔG_{ads}) was defined as

$$\Delta G_{\text{ads}} = G_{\text{adsorbate+surface}} - G_{\text{adsorbate}} - G_{\text{surface}},$$

where G_{surface}, $G_{\text{adsorbate}}$ and $G_{\text{adsorbate+surface}}$ are the free energies of the surface, adsorbate in the gas phase, and adsorbate adsorbed on the surface, respectively. Standard formulas of statistical mechanics were used to calculate the thermodynamic correction including zero-point energy (ZPE), thermal energy and entropy derived from partition functions[47,48]. For surface adsorbates, only vibrational contribution was considered, including ZPE, vibrational thermal energy and vibrational entropy. The ZPE correction is given by

$$E_{\text{ZPE}} = \sum_i \frac{h\nu_i}{2},$$

where h is Plank's constant and ν_i is the vibrational frequency i, which is calculated on the basis of the harmonic oscillators approximation. The standard molar vibrational thermal energy contribution is calculated by

$$U^o_{\text{vib}} = RT \sum_i \frac{\frac{h\nu_i}{k_{\text{B}}}}{e^{\frac{h\nu_i}{k_{\text{B}}T}} - 1},$$

where R is the gas constant and k_{B} is Boltzmann's constant. The standard molar vibrational entropy is calculated using the following expression:

$$S^o_{\text{vib}} = R \sum_i \left[\frac{\frac{h\nu_i}{k_{\text{B}}T}}{e^{\frac{h\nu_i}{k_{\text{B}}T}} - 1} - \ln\left(1 - e^{h\nu_i/k_{\text{B}}T}\right) \right].$$

Therefore, the Gibbs free energies for surface species are obtained by

$$G = E_{\text{total}} + E_{\text{ZPE}} + U^o - \text{TS}^o,$$

where E_{total} refers to the total energy obtained from DFT calculation. To avoid abnormal entropy contribution, frequencies less than 50 cm^{-1} are set to 50 cm^{-1}. The temperature is set as 298.15 K.

Microkinetic simulation

A microkinetic modelling with simplified CO_2-to-CO elementary steps is conducted to study the dependence of CO* coverage with the CO_2 adsorption energy ($G_{\text{ads}}(CO_2{}^*)$) and CO_2 partial pressure ($P(CO_2)$). The following elementary steps are considered:

$$\text{Step 1}: CO_2 + * \leftrightarrow CO_2*$$

$$\text{Step 2}: CO_2* + H^+ + e^- \leftrightarrow COOH*$$

$$\text{Step 3}: COOH* + H^+ + e^- \leftrightarrow CO* + H_2O$$

$$\text{Step 4}: CO* \leftrightarrow CO + *.$$

The corresponding rate equations can be calculated as

$$r_1 = k_1 p_{CO2} \theta_* - k_{-1} \theta_{CO2*}$$

$$r_2 = k_2 c_{H+} \theta_{CO2*} - k_{-2} \theta_{COOH*}$$

$$r_3 = k_3 c_{H+} \theta_{COOH*} - k_{-3} c_{H2O} \theta_{CO*}$$

$$r_4 = k_4 \theta_{CO*} - k_{-4} p_{CO} \theta_*,$$

where r_i is the rate of step i, which is equal to the rate of the forward reaction minus reverse reaction. θ_X is the coverage of the surface species X, and θ_* stands for the coverage of free sites. k_i (k_{-i}) is the rate constant of the forward (reverse) reaction, which can be derived from transition state theory[49]:

$$k = \frac{k_{\text{B}}T}{h} e^{-\Delta G^{\neq,o}/k_{\text{B}}T},$$

where k_{B}, h and T represent the Boltzmann constant, Planck constant and reaction temperature (393 K in this case). $\Delta G^{\neq,o}$ is the change of standard molar Gibbs free energy between the initial and transition state. The steady-state approximation[50] was used to solve the microkinetic model, which assumes that the changes in all the coverages of surface species X are zero at the steady state. Then, along with the normalization condition of surface sites ($\sum_i \theta_i = 1$), we can solve the equations to obtain the turnover frequency. The energies at given applied potential were converted to the RHE scale using the computational hydrogen electrode[49], and then converted to the standard hydrogen electrode scale. $0.5eU$ was used for the effects of applied potential on activation energies, where e represents the elementary charge (electron charge) and U denotes the applied potential (voltage).

The microkinetic simulation and analysis were performed using the CATKINAS code[51–53]. We used 10^{-50} for the AbsTol and $100 \times \varepsilon$ for

RealTol (ε is the epsilon of the machine, which is the minimum distance that MATLAB can recognize). The fsolve function solves a system of equations by minimizing the sum of squares of the components using the Trust-region algorithm. For this, 1,000 decimals were considered, and the convergence criteria were set to be 10^{-100}. The partial pressures of products were set to be 10^{-20} bar, to describe the reaction condition at the beginning of the reaction.

Life cycle assessment

We conducted a cradle-to-gate life cycle assessment to evaluate the GHG emissions from key stages, including air contactor, electrocatalytic processes and pressure-swing adsorption (PSA). The functional unit for this assessment was 1 t of ethylene. Wind energy was utilized in the system. Emission factors for these electricity sources were derived from the Greenhouse Regulated Emissions and Energy use in Technologies (GREET 2023) model[54].

Techno-economic assessment

Detailed assumptions and calculations are provided in the Supplementary Information.

Data availability

The authors declare that all data supporting the findings of this study are available within the Article and its Supplementary Information.

References

1. Birdja, Y. Y. et al. Advances and challenges in understanding the electrocatalytic conversion of carbon dioxide to fuels. *Nat. Energy* **4**, 732–745 (2019).
2. De Luna, P. et al. What would it take for renewably powered electrosynthesis to displace petrochemical processes?. *Science* **364**, eaav3506 (2019).
3. Sullivan, I. et al. Coupling electrochemical CO_2 conversion with CO_2 capture. *Nat. Catal.* **4**, 952–958 (2021).
4. Ethylene market size worth $230.7 billion by 2029|CAGR: 5.5%. *Polaris Market Research* https://www.polarismarketresearch.com/press-releases/ethylene-market (2021).
5. Geyer, R., Jambeck, J. R. & Law, K. L. Production, use, and fate of all plastics ever made. *Sci. Adv.* **3**, e1700782 (2017).
6. Keith, D. W., Holmes, G., St. Angelo, D. & Heidel, K. A process for capturing CO_2 from the atmosphere. *Joule* **2**, 1573–1594 (2018).
7. Welch, A. J., Dunn, E., DuChene, J. S. & Atwater, H. A. Bicarbonate or carbonate processes for coupling carbon dioxide capture and electrochemical conversion. *ACS Energy Lett.* **5**, 940–945 (2020).
8. Li, T. et al. Electrolytic conversion of bicarbonate into CO in a flow cell. *Joule* **3**, 1487–1497 (2019).
9. Li, Y. C. et al. CO_2 electroreduction from carbonate electrolyte. *ACS Energy Lett.* **4**, 1427–1431 (2019).
10. Li, M., Irtem, E., Iglesias van Montfort, H.-P., Abdinejad, M. & Burdyny, T. Energy comparison of sequential and integrated CO_2 capture and electrochemical conversion. *Nat. Commun.* **13**, 5398 (2022).
11. Lee, G. et al. CO_2 electroreduction to multicarbon products from carbonate capture liquid. *Joule* **7**, 1277–1288 (2023).
12. Siegel, R. E., Pattanayak, S. & Berben, L. A. Reactive capture of CO_2: opportunities and challenges. *ACS Catal.* **13**, 766–784 (2023).
13. Dinh, C.-T. et al. CO_2 electroreduction to ethylene via hydroxide-mediated copper catalysis at an abrupt interface. *Science* **360**, 783–787 (2018).
14. Li, F. et al. Molecular tuning of CO_2-to-ethylene conversion. *Nature* **577**, 509–513 (2020).
15. Chen, Y. et al. Efficient multicarbon formation in acidic CO_2 reduction via tandem electrocatalysis. *Nat. Nanotechnol.* **19**, 311–318 (2024).
16. Oener, S. Z., Foster, M. J. & Boettcher, S. W. Accelerating water dissociation in bipolar membranes and for electrocatalysis. *Science* **369**, 1099–1103 (2020).
17. Sasmal, S. et al. Materials descriptors for advanced water dissociation catalysts in bipolar membranes. *Nat. Mater.* **23**, 1421–1427 (2024).
18. Rodellar, C. G. et al. Ion solvation kinetics in bipolar membranes and at electrolyte–metal interfaces. *Nat. Energy* **9**, 548–558 (2024).
19. Bui, J. C. et al. Multi-scale physics of bipolar membranes in electrochemical processes. *Nat. Chem. Eng.* **1**, 45–60 (2024).
20. Wakerley, D. et al. Gas diffusion electrodes, reactor designs and key metrics of low-temperature CO_2 electrolysers. *Nat. Energy* **7**, 130–143 (2022).
21. Gunathunge, C. M. et al. Spectroscopic observation of reversible surface reconstruction of copper electrodes under CO_2 reduction. *J. Phys. Chem. C* **121**, 12337–12344 (2017).
22. Zhan, C. et al. Revealing the CO coverage-driven C–C coupling mechanism for electrochemical CO_2 reduction on Cu_2O nanocubes via operando raman spectroscopy. *ACS Catal.* **11**, 7694–7701 (2021).
23. An, H. et al. Sub-second time-resolved surface-enhanced raman spectroscopy reveals dynamic CO intermediates during electrochemical CO_2 reduction on copper. *Angew. Chem. Int. Ed.* **60**, 16576–16584 (2021).
24. Nørskov, J. K. et al. Trends in the exchange current for hydrogen evolution. *J. Electrochem. Soc.* **152**, J23 (2005).
25. Wang, X. et al. Efficient electrically powered CO_2-to-ethanol via suppression of deoxygenation. *Nat. Energy* **5**, 478–486 (2020).
26. Du, Z.-Y. et al. Promoting water activation via molecular engineering enables efficient asymmetric C–C coupling during CO_2 electroreduction. *J. Am. Chem. Soc.* **146**, 32870–32879 (2024).
27. Yang, R. et al. How local electric field regulates C–C coupling at a single nanocavity in electrocatalytic CO_2 reduction. *Nat. Commun.* **15**, 7140 (2024).
28. Xiao, Y. et al. Asymmetric CO–CHO coupling over Pr single-atom alloy enables industrial-level electrosynthesis of ethylene. *J. Am. Chem. Soc.* **147**, 15654–15665 (2025).
29. Moradzaman, M. & Mul, G. Infrared analysis of interfacial phenomena during electrochemical reduction of CO_2 over polycrystalline copper electrodes. *ACS Catal.* **10**, 8049–8057 (2020).
30. Firet, N. & Smith, W. A. Probing the reaction mechanism of CO_2 electroreduction over Ag films via operando infrared spectroscopy. *ACS Catal.* **7**, 606–612 (2017).
31. Pelayo García de Arquer, F. et al. CO_2 electrolysis to multicarbon products at activities greater than 1 A cm^{-2}. *Science* **367**, 661–666 (2020).
32. Wu, H. et al. Selective and energy-efficient electrosynthesis of ethylene from CO_2 by tuning the valence of Cu catalysts through aryl diazonium functionalization. *Nat. Energy* **9**, 422–433 (2024).
33. Huang, J. E. et al. CO_2 electrolysis to multicarbon products in strong acid. *Science* **372**, 1074–1078 (2021).
34. Zhao, Y. et al. Conversion of CO_2 to multicarbon products in strong acid by controlling the catalyst microenvironment. *Nat. Synth.* **2**, 403–412 (2023).
35. Almajed, H. M. et al. Closing the loop: unexamined performance trade-offs of integrating direct air capture with (bi)carbonate electrolysis. *ACS Energy Lett.* **9**, 2472–2483 (2024).
36. Zhang, B., Lui, Y. H., Ni, H. & Hu, S. Bimetallic $(Fe_xNi_{1-x})_2P$ nanoarrays as exceptionally efficient electrocatalysts for oxygen evolution in alkaline and neutral media. *Nano Energy* **38**, 553–560 (2017).
37. Perdew, J. P., Burke, K. & Ernzerhof, M. Generalized gradient approximation made simple. *Phys. Rev. Lett.* **77**, 3865–3868 (1996).

38. Kresse, G. & Furthmüller, J. Efficiency of ab-initio total energy calculations for metals and semiconductors using a plane-wave basis set. *Comput. Mater. Sci.* **6**, 15–50 (1996).
39. Kresse, G. & Hafner, J. Ab initio molecular-dynamics simulation of the liquid-metal–amorphous-semiconductor transition in germanium. *Phys. Rev. B* **49**, 14251–14269 (1994).
40. Klimeš, J., Bowler, D. R. & Michaelides, A. Van der Waals density functionals applied to solids. *Phys. Rev. B* **83**, 195131 (2011).
41. Kresse, G. & Joubert, D. From ultrasoft pseudopotentials to the projector augmented-wave method. *Phys. Rev. B* **59**, 1758–1775 (1999).
42. Blöchl, P. E., Jepsen, O. & Andersen, O. K. Improved tetrahedron method for Brillouin-zone integrations. *Phys. Rev. B* **49**, 16223–16233 (1994).
43. Montoya, J. H., Shi, C., Chan, K. & Norskov, J. K. Theoretical insights into a CO dimerization mechanism in CO_2 electroreduction. *J. Phys. Chem. Lett.* **6**, 2032–2037 (2015).
44. Stukowski, A. Visualization and analysis of atomistic simulation data with OVITO—the Open Visualization Tool. *Model. Simul. Mater. Sci. Eng.* **18**, 015012 (2010).
45. Alavi, A., Hu, P., Deutsch, T., Silvestrelli, P. L. & Hutter, J. CO oxidation on Pt(111): an ab initio density functional theory study. *Phys. Rev. Lett.* **80**, 3650–3653 (1998).
46. Liu, Z.-P. & Hu, P. General rules for predicting where a catalytic reaction should occur on metal surfaces: a density functional theory study of C–H and C–O bond breaking/making on flat, stepped, and kinked metal surfaces. *J. Am. Chem. Soc.* **125**, 1958–1967 (2003).
47. Wang, Z., Wang, H.-F. & Hu, P. Possibility of designing catalysts beyond the traditional volcano curve: a theoretical framework for multi-phase surfaces. *Chem. Sci.* **6**, 5703–5711 (2015).
48. Wang, Z., Cao, X. M., Zhu, J. & Hu, P. Activity and coke formation of nickel and nickel carbide in dry reforming: A deactivation scheme from density functional theory. *J. Catal.* **311**, 469–480 (2014).
49. Chorkendorff, I. & Niemantsve, J. W. *Concepts of Modern Catalysis and Kinetics* (Wiley-VCH, 2003).
50. Norskov, J. K. et al. Origin of the overpotential for oxygen reduction at a fuel-cell cathode. *J. Phys. Chem. B* **108**, 17886–17892 (2004).
51. Chen, J.-F., Mao, Y., Wang, H.-F. & Hu, P. Reversibility iteration method for understanding reaction networks and for solving microkinetics in heterogeneous catalysis. *ACS Catal.* **6**, 7078–7087 (2016).
52. Chen, J., Jia, M., Lai, Z., Hu, P. & Wang, H. SSIA: A sensitivity-supervised interlock algorithm for high-performance microkinetic solving. *J. Chem. Phys.* **154**, 024108 (2021).
53. Chen, J., Jia, M., Hu, P. & Wang, H. CATKINAS: a large-scale catalytic microkinetic analysis software for mechanism auto-analysis and catalyst screening. *J. Comput. Chem.* **42**, 379–391 (2021).
54. Argonne National Lab. *GREET® Model: The Greenhouse Gases, Regulated Emissions, and Energy Use in Transportation (GREET) Model* (Energy Systems Argonne National Laboratory, 2023).

Acknowledgements

This research received financial support from Saudi Aramco Technologies Company under agreement no. SATC-2022-016. Z.W. acknowledges the Marsden Fund Council from Government funding (21-UOA-237) and Catalyst: Seeding General Grant (22-UOA-031-CGS), managed by Royal Society Te Apārangi. Y.M. and Z.W. acknowledge the use of New Zealand eScience Infrastructure (NeSI) high-performance computing facilities, consulting support and/or training services as part of this research. This work made use of the EPIC facility of Northwestern University's NUANCE Center, which has received support from the SHyNE Resource (NSF ECCS-2025633), the IIN, and Northwestern's MRSEC programme (NSF DMR-2308691). This research used the beamline 9-BM of the Advanced Photon Source, a US Department of Energy (DOE) Office of Science user facility at Argonne National Laboratory and is based on research supported by the US DOE Office of Science-Basic Energy Sciences, under contract no. DE-AC02-06CH11357. This work also acknowledges valuable discussions on data analysis with S. Lee from beamline 12-BM of the Advanced Photon Source.

Author contributions

E.H.S. and K.X. supervised the project. Z.W. supervised the DFT calculations. Y.C. conceived the idea, designed and synthesized materials, conducted the experiments and wrote the manuscript. P.W. assisted in material synthesis, electrocatalytic performance evaluation and material characterization. Y.M. performed the DFT calculations. G.S. conducted techno-economic analysis and life cycle assessment calculations under the supervision of J.B.D. H.L. and L.F. contributed to data analysis and discussions. B.P., Z.L. Y.W. and X.H. contributed to TEM measurements. H.Z. assisted with operando Raman measurements. J.L. and S.L. contributed to XAS measurements and data analysis. A.A., A.J. and I.G. supervised the project and contributed to manuscript preparation. All authors discussed the results and assisted during manuscript preparation.

Competing interests

There is a US provisional patent application titled 'Energy-efficient electrified ethylene production from carbonate capture liquid', filed by the authors Y.C., I.G., A.A., K.X. and E.H.S. of this Article and their institutions. The other authors declare no competing interests.

Additional information

Supplementary information The online version contains supplementary material available at https://doi.org/10.1038/s44160-026-01024-5.

Correspondence and requests for materials should be addressed to Ziyun Wang, Ke Xie or Edward H. Sargent.

Peer review information *Nature Synthesis* thanks Yanqiang Huang and the other, anonymous, reviewer(s) for their contribution to the peer review of this work. Primary Handling Editor: Alexandra Groves, in collaboration with the *Nature Synthesis* team.

[1]Department of Chemistry, Northwestern University, Evanston, IL, USA. [2]Department of Electrical and Computer Engineering, Northwestern University, Evanston, IL, USA. [3]Materials Innovation Factory and Department of Chemistry University of Liverpool, Liverpool, UK. [4]School of Chemical Sciences, The University of Auckland, Auckland, New Zealand. [5]Department of Chemical and Biological Engineering, Northwestern University, Evanston, IL, USA. [6]Department of Materials Science and Engineering, Northwestern University, Evanston, IL, USA. [7]The NUANCE Center, Northwestern University, Evanston, IL, USA. [8]Department of Electrical and Computer Engineering, University of Toronto, Toronto, Ontario, Canada. [9]Research and Development Center, Saudi Aramco, Dhahran, Saudi Arabia. [10]X-ray Science Division, Argonne National Laboratory, Lemont, IL, USA. [11]These authors contributed equally: Yuanjun Chen, Peiying Wang, Yu Mao, Guangcan Su. ✉e-mail: ziyun.wang@auckland.ac.nz; ke-xie@northwestern.edu; ted.sargent@northwestern.edu